Reconstruction of a uniform star object from interior x-ray data: uniqueness, stability and algorithm

Gert Van Gompel[1], Michel Defrise[2] and K Joost Batenburg[1]

[1] IBBT-VisionLab, University of Antwerp, B-2610 Antwerp, Belgium
[2] Department of Nuclear Medicine, Vrije Universiteit Brussel, B-1090 Brussels, Belgium

Abstract

In this paper we consider the problem of reconstructing a two-dimensional star-shaped object of uniform density from truncated projections of the object. In particular, we prove that such an object is uniquely determined by its parallel projections sampled over a full π angular range with a detector that only covers an interior field-of-view, even if the density of the object is not known *a priori*. We analyze the stability of this reconstruction problem and propose a reconstruction algorithm. Simulation experiments demonstrate that the algorithm is capable of reconstructing a star-shaped object from interior data, even if the interior region is much smaller than the size of the object. In addition, we present results for a heuristic reconstruction algorithm called DART, that was recently proposed. The heuristic method is shown to yield accurate reconstructions if the density is known in advance, and to have a very good stability in the presence of noisy projection data. Finally, the performance of the DBP and DART algorithms is illustrated for the reconstruction of real micro-CT data of a diamond.

1. Introduction

This paper concerns the problem of reconstructing an object with uniform density from x-ray projections. In particular, we consider the reconstruction of star-shaped objects from limited projection data, where the detector only covers an interior-field-of-view. Figure 1(a) shows an example of such a star-shaped object, along with a single projection collected by a detector that is significantly smaller than the diameter of the object. We will show that a 2D star-shaped object of uniform but unknown density is determined by its parallel projections sampled over a full π angular range with a detector that only covers an interior field-of-view.

A broad class of similar problems have been analyzed in the past, all aiming at characterizing objects with constant or piecewise constant densities from tomographic data, with applications mainly for non-destructive testing. These problems differ by the nature of the data, by the data sampling and by the class of objects in which a solution is sought. In
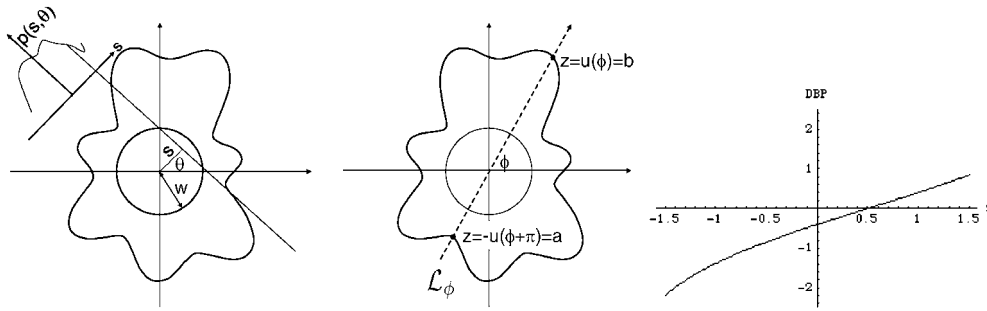
Figure 1. Left: a star object with the interior field-of-view of radius w. The line integrals $p(s, \theta)$ of this object are measured for all lines intersecting the field-of-view, i.e. all lines with $|s| \leqslant w$ and $0 \leqslant \theta < \pi$. Middle: the data derivative $\partial p/\partial s$ is backprojected along a central line $\mathcal{L}_\phi$ through the origin to obtain the DBP $g_\phi(z)$ on the segment $-w \leqslant z \leqslant w$. Right: the radius $b = u(\phi)$ and $-a = u(\phi + \pi)$ of the star object along $\mathcal{L}_\phi$ and its density c are determined by fitting equation (8) to the DBP $g_\phi(z)$, here illustrated for $a = -2$, $b = 3$ and $w = 1.5$.

particular, the problem considered in this paper belongs to the field of *Geometric Tomography*, which focuses on the reconstruction of geometric objects from their sections, orthogonal projections or both [1, 2].

We consider the case where the data consist of x-ray projections: an x-ray projection is the set of integrals of the object along a fan (in 2D) or a cone (in 3D) of lines diverging from a vertex, which corresponds physically to the anode of the x-ray source in CT. Volčič [3] showed for instance that a convex 2D object with known uniform density is determined by x-ray projections measured from any set of three non-collinear vertices not contained within the object. For this result, and most other results in the literature on geometric tomography, it is assumed that the density of the object is known beforehand and that the projections are not truncated in the sense that the integral of the object is measured (or known to be zero) for *all* lines diverging from the vertex. In CT however the density represents the linear attenuation coefficient for x-rays, and an accurate estimate of that quantity can be obtained only if both the nature of the material and the incident x-ray spectrum are known. In addition, especially with micro-CT scanners, the detector is sometimes too small to cover the whole sample and in that case the projections are necessarily truncated. This observation motivates the present study of the *interior problem* for an object with uniform but unknown density. In the interior problem, the integral of the object is measured only for those lines that intersect a circular *field-of-view* (FOV) contained within the support of the object. This corresponds to CT data acquired with a short detector and a 2π rotation of the assembly x-ray source detector. We assume that these data are parameterized as *parallel projections*, where a parallel projection is defined as the set of the integrals of the object along the lines parallel to a direction. This choice of the parametrization does not restrict the generality of the uniqueness theorem in section 4. Note also that interpolating the measured diverging x-ray projections into parallel projections is common practice in many CT systems (see e.g. section 3.7 in [4]).

In medical tomography, the density to be reconstructed is an arbitrary function and in that case the solution of the interior problem is not unique (see theorem 6.5 in [5] and the singular value analysis in [6]). Uniqueness however can be restored if strong prior knowledge is available. For instance, it was shown recently [7, 8] that interior data determine the density function in a unique and stable way within the measured FOV, as soon as this function is known *a priori* in a subset of that FOV. This result is obtained using the *differential backprojection*

(DBP), a powerful tool based on a theorem by Gelfand and Graev (theorem 1 and case $k = 1$ in [9]) and recently exploited to solve several problems in 2D and 3D tomography with incomplete data [10–15]. This paper follows a similar approach based on the DBP to show in section 4 that the interior problem also allows unique reconstruction provided the object is known to be uniform and star shaped (in the sense that each half-line diverging from the center of the FOV has one and only one intersection with the boundary of the object support). A stability estimate is obtained in section 6 using the Cramer–Rao bound.

The major goal of this paper is to prove these new uniqueness and stability results for the reconstruction of a star object from interior data. Interestingly however, the proof leads directly to a reconstruction algorithm, denoted as the DBP algorithm and described in section 7. As discussed above, this algorithm requires that the object has a uniform density. This assumption is restrictive, not only because it prevents the application to piecewise uniform samples containing different materials but also because of confounding physical effects such as beam hardening. An alternative approach consists in encouraging rather than strictly enforcing piecewise uniformity. This can be done using penalized maximum-likelihood algorithms for image reconstruction, with various types of penalties which favor sparse solutions in some appropriate basis. For instance Candes *et al* [17], Sidky *et al* [18] and Herman and Davidi [19] have shown that the total-variation penalty allows very accurate reconstructions of fairly complex piecewise objects from a very small number of projections. Another alternative to the DBP algorithm is the discrete algebraic reconstruction technique (DART) proposed in [16]. This algorithm requires a uniform object with known density, but avoids the hypothesis that the object must be star shaped. In section 8 we apply the DBP and the DART algorithms and illustrate their performance for the reconstruction of simulated data and of real micro-CT data of a diamond.

2. Notation and concepts

Let $\mathbb{R}_{>0} = \{x \in \mathbb{R} : x > 0\}$. Let $\mathcal{J}$ be the class of finite and integrable functions $f : \mathbb{R}^2 \to \mathbb{R}$ with a compact support for which the Radon transform

$$p(s, \theta) = (\mathcal{R}f)(s, \theta) = \int_{-\infty}^{\infty} f(s \cos\theta - t \sin\theta, s \sin\theta + t \cos\theta) \, \mathrm{d}t \qquad (1)$$

is defined almost everywhere in $s \in \mathbb{R} \times 0 \leqslant \theta < \pi$, with the symmetry $p(s, \theta) = p(-s, \theta + \pi)$. The variables s and θ are the usual sinogram variables: s is the signed distance between the line and the origin of the coordinate system, and θ defines the line orientation as shown in figure 1.

Let $O = (0, 0)$. A set $S \subset \mathbb{R}^2$ is called *star shaped* at O if every line through O that meets S does so in a line segment. By $\mathcal{S}$, we denote the collection of nonempty, compact sets that are star shaped at O and for which O is an interior point. Let $S \in \mathcal{S}$. The *radial function* $\rho_S : \mathbb{R}^2 \to \mathbb{R}_{>0}$ of S is defined by

$$\rho_S(x, y) = \max\{h : (hx, hy) \in S\}. \qquad (2)$$

The radial function is often restricted to the unit circle. Switching to polar coordinates, it can then be represented by a periodic function $u_S : \mathbb{R} \to \mathbb{R}_{>0}$ with period 2π, such that for $r > 0$ and $0 \leqslant \phi < 2\pi$:

$$(r \cos\phi, r \sin\phi) \in S \iff r \leqslant u_S(\phi). \qquad (3)$$

We call a star-shaped set S a *star object* if u_S is a continuous function. Let S be a star object and let $c \in \mathbb{R}$. Define a *star object of density c* by

$$f_{S,c}(r \cos\phi, r \sin\phi) = \tilde{f}_{S,c}(r, \phi) = \begin{cases} c & r \leqslant u_S(\phi) \\ 0 & r > u_S(\phi) \end{cases}, \qquad (4)$$

3

where $\tilde{f}_{S,c}$ corresponds to the polar coordinate representation of $f_{S,c}$. Note that the term *star object* will be used to refer to either the star-shaped set or its representation as a function, depending on context. The set of all functions $f_{S,c}$, where S is a star object and $c \in \mathbb{R}$ is denoted by $\mathcal{F}$. From now on, we omit the index S, c and S for the functions f and u.

It is well known that under very general assumptions (theorem 1.7 in [27]), any function in $\mathcal{J}$ is uniquely determined by its Radon transform. In this paper we consider the problem of reconstructing a star object from only part of its Radon transform, corresponding to a detector for which the field-of-view covers only part of the interior of the object. We prove the following uniqueness theorem.

Theorem 1 (Uniqueness theorem). *Let $w > 0$. Every function $f \in \mathcal{F}$ is uniquely determined, among all $g \in \mathcal{F}$, by the value $p(s, \theta)$ of its Radon transform on the set $|s| \leqslant w, 0 \leqslant \theta < \pi$.*

Note that we do not assume central symmetry, i.e. we do not assume that the radial function u satisfies $u(\phi) = u(\phi + \pi)$. This uniqueness theorem will be proved in section 4. As the proof is constructive, it also leads to an algorithm for solving the following reconstruction problem.

Problem 1 (Reconstruction problem for unknown density). *Let $w > 0$. Suppose that the Radon transform $p(s, \theta)$ of $f \in \mathcal{F}$ is given for $|s| \leqslant w$ and $0 \leqslant \theta < \pi$. Compute f from this partial Radon transform.*

In section 6, we will show that the solution of Problem 1 can be quite unstable. Stability can be significantly improved if the density of f is known *a priori*. This leads to the following reconstruction problem, which fits perfectly in the domain of geometric tomography:

Problem 2 (Reconstruction problem for known density). *Let S be a star object, let f be the indicator function of S and let $w > 0$. Suppose that the Radon transform $p(s, \theta)$ of f is given for $|s| \leqslant w$ and $0 \leqslant \theta < \pi$. Compute f from this partial Radon transform.*

3. The differential backprojection and the Hilbert transform

We introduce in this section the differential backprojection (DBP). Let $f \in \mathcal{J}$ be a finite and integrable function with a compact support, and let $p(s, \theta)$ be its Radon transform. Consider a fixed direction $0 \leqslant \phi < \pi$ and the central line $\mathcal{L}_\phi = \{(z \cos \phi, z \sin \phi), z \in \mathbb{R}\}$. For each point z along this line define the backprojection of the derivative of the Radon transform:

$$g_\phi(z) = \frac{-1}{2} \int_0^\pi \text{sgn}(\cos(\theta - \phi)) \left. \frac{\partial p(s, \theta)}{\partial s} \right|_{s = z \cos(\theta - \phi)} d\theta. \qquad (5)$$

This function is defined almost everywhere in $z \in \mathbb{R}$ because the derivative $\partial p / \partial s$ of the Radon transform of $f \in \mathcal{J}$ can be defined almost everywhere. If necessary, it can be defined as a distribution (see chapter 10 in [20] for the definition of the Radon transform of distributions and section 4.1 in [21] for the definition of the DBP and Hilbert transform of functions in $L_0^2(\mathbb{R}^2)$).

Noo *et al* [10] and Zou *et al* [11] have shown that the DBP function in equation (5) is related to the Hilbert transform of f along $\mathcal{L}_\phi$ by

$$g_\phi(z) = (\mathcal{H} f_\phi)(z) = p.v. \int_{-\infty}^\infty \frac{1}{z - z'} f_\phi(z') \, dz' \qquad z \in \mathbb{R}, \qquad (6)$$

where $p.v.$ denotes the Cauchy principal value and f_ϕ is the restriction of f to $\mathcal{L}_\phi$:

$$f_\phi(z) = f(z \cos \phi, z \sin \phi) = \begin{cases} \tilde{f}(|z|, \phi) & z \geqslant 0 \\ \tilde{f}(|z|, \phi + \pi) & z < 0 \end{cases} \tag{7}$$

with $\tilde{f}$ being the polar coordinate representation of f. To simplify notations our definition (6) of the Hilbert transform $\mathcal{H}$ differs from the standard definition by a factor π. Note that the DBP separates the 2D problem into a set of independent 1D problems along a family of central lines $\mathcal{L}_\phi$. The usefulness of the DBP stems from the existence of a closed form expression (equation (12) p 175 in [22]) for the *inverse finite Hilbert transform*, which allows recovering a function $f_\phi(z)$ that vanishes outside the interval $(-1, 1)$ from its Hilbert transform $g_\phi(z)$ on $z \in [-1, 1]$.

4. Uniqueness for star objects

In this section we prove theorem 1 in a constructive manner. The proof will also provide the basis of a reconstruction algorithm, described in section 7.

We will show that for any $w > 0$ the star object (4) can be reconstructed in a unique way from its Radon transform $p(s, \theta)$, measured over the region $|s| \leqslant w, 0 \leqslant \theta < \pi$. The line integrals of f in (1) are measured for all lines that intersect a circular field-of-view of radius w centered at $x = y = 0$, where the parameter w is determined by the size of the detector. Note that the field-of-view can be centered at any point such that each half-line diverging from this point has only one intersection with the boundary of the support of f. Without loss of generality we assume that $u(\phi) > w$ for $0 \leqslant \phi < 2\pi$, the problem is then referred to as an *interior problem*. This assumption is not restrictive since w can always be decreased until an interior problem is obtained.

To prove theorem 1, we use the differential backprojection (DBP). For the specific case of the star object, inserting (7) into (6) and using (4) yields

$$\begin{aligned} g_\phi(z) &= -c \log(u(\phi) - z) + c \log(z + u(\phi + \pi)) & -w < z < w \\ &= -c \log(b - z) + c \log(z - a), \end{aligned} \tag{8}$$

where we have defined the end points $a = -u(\phi + \pi)$ and $b = u(\phi)$ of the support of f_ϕ (i.e., the support of f along the line $\mathcal{L}_\phi$) and we omit the dependence of a and b on ϕ to simplify notations. Note that $a < -w$ and $b > w$ because the interior field-of-view of radius w is contained within the support of f.

In practice one would estimate the three parameters a, b, c using typically a least-square fit of the RHS of (8) to the DBP $g_\phi(z)$ on the segment $z \in [-w, w]$ where it can be recovered from the interior data. To prove uniqueness however, we are not concerned by stability, and we simply consider the first and second derivatives of the Hilbert transform

$$\begin{aligned} g'_\phi(z) &= \frac{\mathrm{d}g_\phi(z)}{\mathrm{d}z} = \frac{c}{b - z} + \frac{c}{z - a}, \\ g''_\phi(z) &= \frac{\mathrm{d}^2 g_\phi(z)}{\mathrm{d}z^2} = \frac{c}{(b - z)^2} - \frac{c}{(z - a)^2}, \end{aligned} \tag{9}$$

which are continuous on $-a < -w \leqslant z \leqslant w < b$, with $g'_\phi(z) > 0$. An additional equation is given by the integral of f along $\mathcal{L}_\phi$, which is measured because that central line intersects the field-of-view. This integral is equal to $p(0, \phi - \pi/2) = c(b - a)$. Using (9), one obtains

$$a + b = \frac{-p(0, \phi - \pi/2)g''_\phi(0)}{(g'_\phi(0))^2}, \tag{10}$$

5

$$ab = \frac{-p(0, \phi - \pi/2)}{g'_\phi(0)}.$$

(11)

If the data are consistent the system (10), (11) has a unique solution such that $b > 0$ and $a < 0$. The object density is then recovered as

$$c = p(0, \phi - \pi/2)/(b - a).$$

(12)

This concludes the proof of theorem 1.

5. Generalizations

Theorem 1 has been obtained for the parallel-beam parametrization of the 2D Radon transform, equation (1). Extension to the 2D fan-beam parametrization is straightforward by resampling the fan-beam data into parallel-beam data, as is often done in CT. Alternatively, it is possible to avoid this resampling by exploiting instead of equation (5) a similar equation that directly relates the Hilbert transform of f to the backprojection of its differentiated fan-beam data (see [14] and equation (24) in [12]). That relation also holds for the 3D x-ray transform and could therefore be applied for a spiral data acquisition with a multi-row CT scanner.

The uniqueness theorem for the interior problem with star objects can also be extended to more general classes of objects. Note first that equations (5) and (6) are valid for arbitrary density functions in $\mathcal{J}$. Applying the same approach as in the previous section to a class of objects which can be described along each line $\mathcal{L}_\phi$ by J parameters $a_{j,\phi}$, $j = 1, \ldots, J$, the interior problem is reduced to estimating these parameters by fitting the function $g_\phi(z)$ that has been recovered on $z \in [-w, w]$ using the DBP. Uniqueness should then be verified for each type of parametrization. More generally, we conjecture that a uniqueness theorem might be obtained for general binary objects by using the analyticity lemma 2.1 of [26]. It is likely however that the stability with respect to measurement noise will rapidly degrade with objects of increased complexity. Therefore, we restrict our attention to star objects in the rest of the paper.

6. Stability

The stability of the inverse problem in the previous section can be analyzed by calculating for each radial line $\mathcal{L}_\phi$ the Cramer–Rao lower bound (see e.g. section 13.3.5 in [23]) for the variance of an unbiased estimator of the parameters $a = -u(\phi + \pi)$ and $b = u(\phi)$. Recall that an estimator $\hat{a}$ of the parameter a is unbiased if its expectation $E(\hat{a})$ is equal to a. We derive this Cramer–Rao lower bound under the following assumptions:

- The DBP $g_\phi(z)$ calculated using (5) is a white Gaussian stochastic process on $-w \leqslant z \leqslant w$, with mean value given by (8) and with uniform variance σ^2,
- The ray-sum $p(0, \phi - \pi/2)$ along $\mathcal{L}_\phi$ is a Gaussian random variable with mean value $c(b - a)$ and with variance σ_p^2.
- There is no correlation between the noise on $p(0, \phi - \pi/2)$ and on $g_\phi(z)$.

The logarithm of the likelihood function is then

$$L(g, p | a, b, c) = \frac{-1}{2\sigma_p^2}(p(0, \phi - \pi/2) - c(b - a))^2$$

(13)

$$-\frac{1}{2\sigma^2}\int_{-w}^{w}(g_\phi(z) + c\log(b - z) - c\log(z - a))^2 \, \mathrm{d}z.$$

(14)

The Fisher matrix for the three parameters a, b and c is

$$F = \begin{pmatrix} F_{a,a} & F_{a,b} & F_{c,a} \\ F_{a,b} & F_{b,b} & F_{c,b} \\ F_{c,a} & F_{c,b} & F_{c,c} \end{pmatrix}, \tag{15}$$

with

$$F_{a,a} = -E\left(\frac{\partial^2 L}{\partial a^2}\right) = \frac{c^2}{\sigma_p^2} + \frac{1}{\sigma^2}\int_{-w}^{w}\frac{c^2}{(z-a)^2}\,\mathrm{d}z = \frac{c^2}{\sigma_p^2} + \frac{2c^2 w}{\sigma^2(a^2-w^2)},$$

$$F_{a,b} = -E\left(\frac{\partial^2 L}{\partial a\partial b}\right) = \frac{-c^2}{\sigma_p^2} + \frac{1}{\sigma^2}\int_{-w}^{w}\frac{c^2}{(z-a)(b-z)}\,\mathrm{d}z$$

$$= \frac{-c^2}{\sigma_p^2} + \frac{c^2}{\sigma^2(a-b)}\log\left\{\frac{(a+w)(w-b)}{(w-a)(b+w)}\right\},$$

$$F_{b,b} = -E\left(\frac{\partial^2 L}{\partial b^2}\right) = \frac{c^2}{\sigma_p^2} + \frac{1}{\sigma^2}\int_{-w}^{w}\frac{c^2}{(b-z)^2}\,\mathrm{d}z = \frac{c^2}{\sigma_p^2} + \frac{2c^2 w}{\sigma^2(b^2-w^2)},$$

$$F_{c,c} = -E\left(\frac{\partial^2 L}{\partial c^2}\right) = \frac{(b-a)^2}{\sigma_p^2} + \frac{1}{\sigma^2}\int_{-w}^{w}(\log(b-z)-\log(z-a))^2\,\mathrm{d}z,$$

$$F_{c,a} = -E\left(\frac{\partial^2 L}{\partial c\partial a}\right) = \frac{c(a-b)}{\sigma_p^2} + \frac{1}{\sigma^2}\int_{-w}^{w}(\log(b-z)-\log(z-a))\,\frac{c}{z-a}\,\mathrm{d}z,$$

$$F_{c,b} = -E\left(\frac{\partial^2 L}{\partial c\partial b}\right) = \frac{c(b-a)}{\sigma_p^2} + \frac{1}{\sigma^2}\int_{-w}^{w}(\log(b-z)-\log(z-a))\,\frac{c}{b-z}\,\mathrm{d}z, \tag{16}$$

where $E()$ denotes the expectation value. The variance of any unbiased estimator $\hat{a}$, $\hat{b}$, $\hat{c}$ of the three parameters is then bounded below by the diagonal elements of the inverse Fisher matrix

$$\text{Var}\,\hat{a} \geqslant (F^{-1})_{a,a}, \qquad \text{Var}\,\hat{b} \geqslant (F^{-1})_{b,b}, \qquad \text{Var}\,\hat{c} \geqslant (F^{-1})_{c,c}. \tag{17}$$

When the density c is known beforehand, the lower bound on the variance of $\hat{a}$ and $\hat{b}$ is obtained by calculating the inverse of the 2×2 Fisher matrix

$$F = \begin{pmatrix} F_{a,a} & F_{a,b} \\ F_{a,b} & F_{b,b} \end{pmatrix}, \tag{18}$$

with the same matrix elements as in equation (16).

As an illustration, figure 2 shows the lower bound for the variance of $\hat{a}$ as a function of the radius w of the field-of-view, when the true values of the parameters are $a = -2, b = 3$ and $c = 1$, and the variances are $\sigma^2 = \sigma_p^2 = 1$. For this example, the variance increases dramatically when the radius of the field-of-view, w, is small, which could be expected. In contrast, the variance bound is small when $w \to |a| = 2$: in that limit the field-of-view approaches the corresponding boundary of the support of f along the line $\mathcal{L}_\phi$. The localization of that boundary (a in this example) is easy to determine in this limit because the Hilbert transform is singular at $w = -a$. This can also be seen by noting from equation (16) that $F_{a,a} \to \infty$ when $w \to |a|$. Another expected observation in figure 2 is that the variance bound is much better when the density c is known *a priori*.

Figure 3 shows the value of $F_{b,c}^{-1}\big/\sqrt{F_{b,b}^{-1} F_{c,c}^{-1}}$ as a function of σ_p. This quantity is equal to the asymptotic value of the correlation coefficient between the maximum-likelihood estimators of b and of c. Intuitively one expects this correlation coefficient to be negative, i.e. one expects
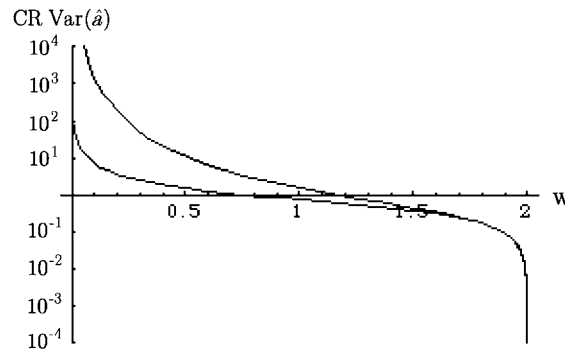
Figure 2. Cramer–Rao lower bound for the variance of an unbiased estimator of the boundary $\hat{a}$, assuming a Gaussian distribution with variance 1 for the Hilbert transform data $g_\phi(z)$ and for the ray sum $p(0, \phi - \pi/2)$. Logarithmic vertical scale for the Cramer–Rao variance bound. Horizontal axis: the radius of the field-of-view w. The true values of the parameters are $a = -2$, $b = 3$ and $c = 1$. The lower curve corresponds to the case where the density c is known. The upper curve corresponds to the case where c is unknown.
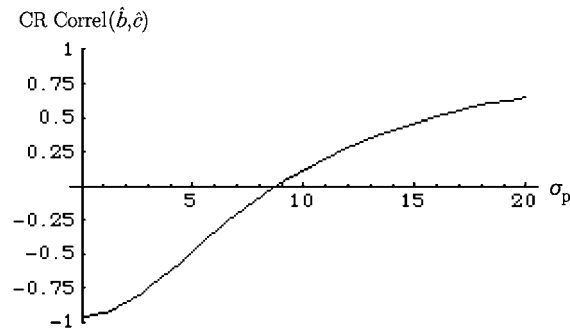
Figure 3. Asymptotic Cramer–Rao value for the correlation coefficient between the estimator of $\hat{b}$ and of the density $\hat{c}$, assuming a Gaussian distribution with variance 1 for the Hilbert transform data $g_\phi(z)$ and with variance σ_p^2 for the ray sum $p(0, \phi - \pi/2)$. Horizontal axis: the value of σ_p. The true values of the parameters are $a = -2$, $b = 3$ and $c = 1$, and the width of the FOV is $w = 1$.

that the estimated density tends to increase when the estimated object shrinks. However, when the variance σ_p^2 on the measured value of the ray-sum is large, figure 3 reveals the counter-intuitive result that the correlation coefficient is positive.

To conclude this section, we stress that the stability estimates above have been obtained by considering separately each radial line $\mathcal{L}_\phi$. Intrinsically the problem is two-dimensional and it is therefore likely that better variance bounds could be obtained by handling the full interior data set $\{p(s, \theta), |s| \leqslant w, 0 \leqslant \theta < \pi\}$ simultaneously. Another limitation is our assumption of white noise on the DBP $g_\phi(z)$: this is at best an approximation because noise correlations are introduced when calculating the DBP (5) from the measured data $p(s, \phi)$.

7. Algorithms

7.1. The DBP algorithm for problems 1 and 2

The Cramer–Rao bound suggests that the reconstruction of a star object from interior data can be rather unstable. To improve the stability, we propose a two-step reconstruction, which is

not optimized but at least partially alleviates the sub-optimality due to the separate handling of each radial line: in a first step an estimate of the density c is obtained for each radial line $\mathcal{L}_\phi$ by using equation (10)–(12), with values of $g'_\phi(0)$ and $g''_\phi(0)$ estimated by fitting a polynomial to the DBP $g_\phi(z)$ on $-w \leqslant z \leqslant w$. The estimated density is then averaged over all radial lines, and that average value is used as a known density during a second step in which only the boundaries a and b are to be determined. If the Gaussian noise assumptions made when deriving the Cramer–Rao bound are valid, and if the variances σ^2 and σ_p^2 are known, maximum-likelihood estimates can be obtained by maximizing the log-likelihood function (14):

$$(\hat{a}, \hat{b}) = \arg \max_{a<0,b>0} L(g, p|a, b, c). \tag{19}$$

Noting that the statistical properties of $g_\phi(z)$ are unknown and probably complex, we have implemented instead the following weighted least square method, which is simpler and avoids the nonlinear optimization of $L(g, p|a, b, c)$. Using the known value of the density c, we define the function

$$h_\phi(z) = \mathrm{e}^{-g_\phi(z)/c}, \tag{20}$$

with g_ϕ being the DBP computed from the measured projections $p(\theta, s)$ using equation (5), and estimate the parameters a and b by minimizing

$$\Psi_\phi(a, b) = \int_{-w}^{w} \left(h_\phi(z) - \frac{b-z}{z-a} \right)^2 (z-a)^2 \, \mathrm{d}z + \int_{-w}^{w} \left(h_\phi^{-1}(z) - \frac{z-a}{b-z} \right)^2 (b-z)^2 \, \mathrm{d}z$$

$$+ \frac{2w}{c^2}\beta \left(p(0, \phi - \pi/2) - c(b-a) \right)^2. \tag{21}$$

This is a least-square fit with weighting factors $(z-a)^2$ and $(b-z)^2$. These weights are not optimal in terms of noise but are chosen for simplicity because they lead to a quadratic cost function (21), and therefore to a closed form solution. The parameter $\beta \geqslant 0$ in equation (21) determines the weight given to the ray-sum data $p(0, \phi - \pi/2)$. Typically one would select a small value of β when the uncertainty on $p(0, \phi - \pi/2)$ is large compared to the uncertainty on the DBP $g_\phi(z)$ (i.e., when the parameter σ_p in the stability study of section 6 is large). The parameters $\hat{a}$ and $\hat{b}$ that minimize $\Psi_\phi(a, b)$ are the solutions of the 2×2 linear system

$$\begin{pmatrix} \int_{-w}^{w} \left(h_\phi^2(z) + 1 \right) \mathrm{d}z + 2w\beta & \int_{-w}^{w} \left(h_\phi(z) + h_\phi^{-1}(z) \right) \mathrm{d}z - 2w\beta \\ \int_{-w}^{w} \left(h_\phi(z) + h_\phi^{-1}(z) \right) \mathrm{d}z - 2w\beta & \int_{-w}^{w} \left(h_\phi^{-2}(z) + 1 \right) \mathrm{d}z + 2w\beta \end{pmatrix} \begin{pmatrix} \hat{a} \\ \hat{b} \end{pmatrix} = \begin{pmatrix} q_a \\ q_b \end{pmatrix}, \tag{22}$$

with

$$\begin{pmatrix} q_a \\ q_b \end{pmatrix} = \begin{pmatrix} \int_{-w}^{w} z \left(h_\phi^2(z) + 1 + h_\phi(z) + h_\phi^{-1}(z) \right) \mathrm{d}z - \frac{2w}{c}\beta p(0, \phi - \pi/2) \\ \int_{-w}^{w} z \left(h_\phi^{-2}(z) + 1 + h_\phi(z) + h_\phi^{-1}(z) \right) \mathrm{d}z + \frac{2w}{c}\beta p(0, \phi - \pi/2) \end{pmatrix}. \tag{23}$$

In summary the algorithm applied in section 8 for Problem 1 consists of the following steps:

(i) Estimate the derivative $\partial p(s, \theta)/\partial s$ (we use a two-point difference estimate with a half-sample shift).

(ii) Using (5), backproject on a family of radial lines to obtain the DBP $g_\phi(z)$, $|z| \leqslant w, 0 \leqslant \phi < \pi$.

(iii) For noisy data, smooth $g_\phi(z)$ by applying a Gaussian filter along the angular variable ϕ.

(iv) For each radial line $\mathcal{L}_\phi$:

 • Fit a polynomial to $g_\phi(z)$ to estimate $g'_\phi(0)$ and $g''_\phi(0)$ (we empirically found that a polynomial of degree 5 is sufficient to accurately describe $g_\phi(z)$ for $|z| \leqslant w$).

9
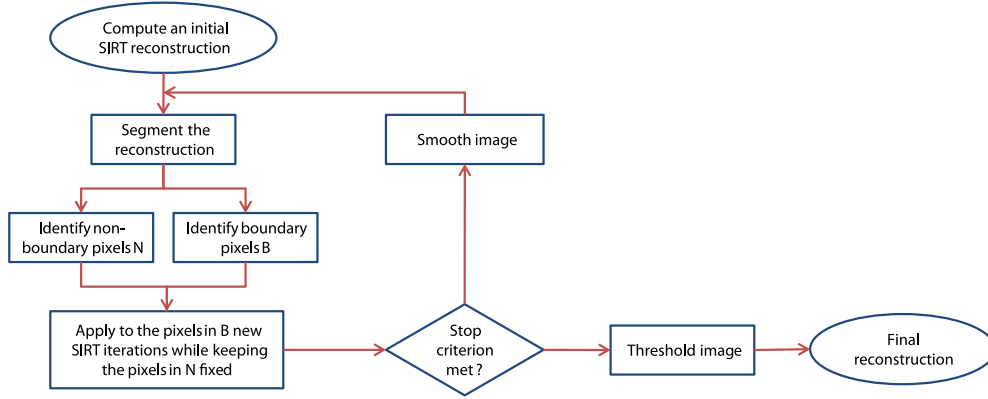
Figure 4. Flow chart of the DART algorithm.

- Apply equation (11) and (12) to obtain an estimate $\hat{c}_\phi$ of the object density.

(v) Calculate the average density estimate $\hat{c} = 1/\pi \int \hat{c}_\phi \, d\phi$.

(vi) Using $\hat{c}$ as the true density, calculate the function h_ϕ in (20) and solve for each radial line the system (22) to obtain an estimate of $a = -u(\phi + \pi)$ and $b = u(\phi)$.

For problem 2, the density is known beforehand and the same algorithm is used, skipping steps iv and v.

7.2. The discrete algebraic reconstruction technique (DART) for problem 2

The differential backprojection leads to the uniqueness theorem 1 and allows one to transform the 2D inverse problem into a set of 1D problems along radial lines $\mathcal{L}_\phi$. This separation is numerically efficient but is unlikely to optimally exploit the data, especially in the presence of noise. This limitation is only partially overcome by the two-step approach in the DBP algorithm of section 7.1.

Algorithms that are intrinsically two dimensional are expected to yield a better stability in the presence of noise. Various algorithms could be considered, for example total variation minimization [18] or the *discrete algebraic reconstruction technique* (DART) [16], which is an algorithm that can be applied to reconstruct any uniform object with a known density.

As an illustration, we implemented the DART method [16] and applied it on the data, assuming that the density c is known (problem 2). The improved stability is illustrated in the next section. In the remainder of this section we describe the variant of DART that we used for the experiments in section 8. For other variants of this algorithm and more details on the underlying algorithmic ideas we refer to [16]. Note that although DART yields strong experimental results, the algorithm is heuristic in nature and does not guarantee convergence.

A high level flow chart of DART is shown in figure 4. DART relies on an underlying reconstruction algorithm for continuous tomography, which is repeatedly used as a subroutine. In this paper, we use SIRT (see e.g. section 5.3 in [5]) as the continuous method.

First, an initial reconstruction $f^{(1)}$ is computed using SIRT. Subsequently, several DART-iterations are performed. In each iteration $n = 1, 2, \ldots$, following steps are executed:

(i) The current reconstruction $f^{(n)}$ is segmented using a simple threshold method, forming the image $t^{(n)}$:

$$t^{(n)}(x, y) = \begin{cases} c & \forall (x, y) \in \Omega : f^{(n)}(x, y) \geqslant \frac{c}{2} \\ 0 & \forall (x, y) \in \Omega : f^{(n)}(x, y) < \frac{c}{2} \end{cases}. \tag{24}$$

(ii) The imaging region Ω is divided into two disjoint subregions: boundary and non-boundary pixels. Let $M(x, y)$ denote the set of at most eight neighboring pixels of $(x, y) \in \Omega$. The set $B^{(n)}$ of boundary pixels is defined as the set of all pixels (x, y) such that the segmented image $t^{(n)}$ is not constant within the neighborhood $M(x, y)$ of (x, y):

$$B^{(n)} = \{(x, y) \in \Omega \,|\, \exists (x', y') \in M(x, y) : t^{(n)}(x', y') \neq t^{(n)}(x, y)\}. \tag{25}$$

The set of non-boundary pixels is defined as $N^{(n)} = \Omega \backslash B^{(n)}$.

(iii) Next, three SIRT iterations are performed exclusively on the set of boundary pixels. The non-boundary pixels are kept fixed at their thresholded values, as given by the image $t^{(n)}$. To this end, the 2D Radon transform of $t_{N^{(n)}}^{(n)}(x, y) = t^{(n)}(x, y) \mathbf{1}_{N^{(n)}}(x, y)$ is calculated and subtracted from the projection data p to obtain modified projection data $p^{(n)}(s, \theta) = p(s, \theta) - \left(\mathcal{R} t_{N^{(n)}}^{(n)}\right)(s, \theta)$ for $|s| \leqslant w, 0 \leqslant \theta < \pi$.

A function $h_{B^{(n)}}^{(n)}$ with support in the region $B^{(n)}$ is computed by applying SIRT to the data $p^{(n)}$. The image $h_{B^{(n)}}^{(n)}$ is then merged with the image $t_{N^{(n)}}^{(n)} = t^{(n)} \mathbf{1}_{N^{(n)}}$, forming the image $h^{(n)}$.

(iv) As a means of regularization, the image $h^{(n)}$ is then blurred using a simple weighted sum, forming $f^{(n+1)}$:

$$f^{(n+1)}(x, y) = 0.95 h^{(n)}(x, y) + 0.05 \sum_{(x', y') \in M(x, y)} \frac{h^{(n)}(x', y')}{|M(x, y)|}, \tag{26}$$

with $|M(x, y)|$ the number of pixels in the neighborhood $M(x, y)$.

After $T = 1000$ DART-iterations, the algorithm terminates and the current reconstruction $f^{(1001)}$ is thresholded, forming the binary reconstruction $t^{(1001)}$.

8. Numerical examples with simulated data

The star object in figure 5 has a density $c = 1$ and a radial function

$$u(\phi) = 40 \left(2 + 0.4 \cos(2\phi) + 0.3 \sin(3\phi + \pi/3) - 0.33 \cos(7\phi - \pi/6)\right). \tag{27}$$

We generated a digital image of this object on a 1024×1024 matrix with pixel size 0.25. Parallel projections $p(s, \theta)$ were calculated for 256 uniformly spaced angular samples over $[0, \pi)$ and with radial sampling $\Delta s = 1.0$, by forward projecting the 1024×1024 image using Joseph's algorithm with linear interpolation [24]. The object was reconstructed on a 256×256 matrix with pixel size 1.0. We considered both the case of unknown and of known density. In the latter case, the data were reconstructed both with the DBP and with the DART algorithm. The accuracy of the reconstructions was quantified by the ratio of the area of the symmetric difference between the estimated object and true object, and the area of the true object

$$\epsilon = \frac{\text{Area} \{\text{supp}(\hat{f}) \,\triangle\, \text{supp}(f)\}}{\text{Area} \{\text{supp}(f)\}}, \tag{28}$$

where supp (f) denotes the support of object function f. The error ϵ varies in the range $[0, \infty)$, where $\epsilon = 0$ represents the ideal case and $\epsilon = 1$ the case when $\hat{f}$ is zero everywhere.

For the DBP algorithm, $g_\phi(z)$ was calculated for the same 256 uniformly spaced angular samples over $\phi \in [0, \pi)$, and for N_z values of z uniformly sampled over $[-w, w]$, with sampling distance $\Delta z = 1.0$ so that $w = N_z/2$.
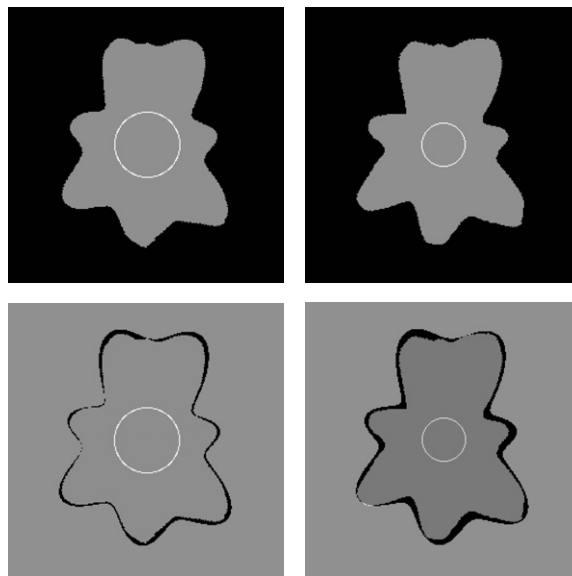
Figure 5. The simulated star object.
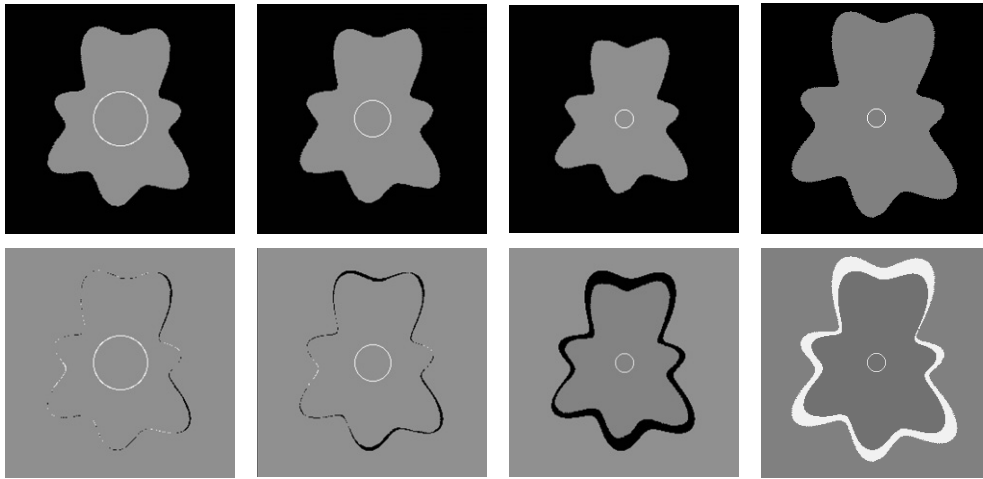
Figure 6. DBP reconstructions from noise-free data using the algorithm of section 7.1. The object density is unknown. The first three columns correspond from left to right to FOV diameters $N_z = 60, 40, 20$, with estimated densities equal to $\hat{c} = 1.006, 0.997$ and 0.892 respectively, using $\beta = 0$. In the fourth column, $N_z = 20$ and $\hat{c} = 0.892$ are the same as in the third column, but $\beta = 0.2$. The interior FOV used for reconstruction is shown as a superimposed white circle. Upper row: the reconstructed star object. Bottom row: difference between the reconstruction and the true object of figure 5.

8.1. Problem 1: unknown density

The object with unknown density is reconstructed using the 2-step DBP algorithm. The first three columns in figure 6 show the reconstructed images for different values of the FOV radius, $N_z = 60, 40, 20$, using $\beta = 0$ and without angular filtering. The FOV circular boundary has been superimposed on the reconstruction. The difference with the true object illustrates the expected degradation of the algorithm accuracy with a decreasing FOV. Even though the simulated data were noise-free for this example, discretization as well as numerical round

12

Figure 7. DBP reconstructions from noisy data using the algorithm of section 7.1. The density is unknown. The columns correspond to FOV diameters $N_z = 60, 40$ with estimated densities equal to $\hat{c} = 0.973$ and 0.812, respectively. Upper row: the reconstructed star object (FOV superimposed). Bottom row: difference between the reconstruction and the true object of figure 5.

off errors have an effect similar to that of random noise, and the results in figure 6 illustrate the poor stability of the DBP algorithm when the FOV is small. The density c estimated by the algorithm was respectively $\hat{c} = 1.006$, $\hat{c} = 0.997$ and $\hat{c} = 0.892$ for $N_z = 60, 40$ and 20. The ratio ϵ was respectively equal to 0.019, 0.047 and 0.233.

From the images in the third column of figure 6, one notes that the values $-\hat{a}$ and $\hat{b}$ are underestimated if $\hat{c}$ is underestimated. For an explanation we refer to figure 3 and the corresponding discussion in section 6, which show that there is a positive correlation between $-\hat{a}$ and $\hat{b}$ on one hand, and $\hat{c}$ on the other hand when σ_p is large, which, as noted above, corresponds to small values of β. To illustrate the impact of the parameter β, the images in the fourth column of figure 6 show the reconstruction for $N_z = 20$ with $\beta = 0.2$. In this case, the underestimation of $\hat{c} = 0.892$ is paired with an overestimation of $-\hat{a}$ and $\hat{b}$, as expected from the fact that the correlation in figure 3 is negative for small σ_p.

To illustrate the stability of the algorithm, pseudo-random Poisson noise was added to the sinogram, corresponding to a total of one million photons; this resulted in a relative standard deviation of 0.005 for the largest sinogram sample. Figure 7 shows the reconstructions for $N_z = 60$ and $N_z = 40$, done with a filtering of the DBP data with an angular Gaussian filter of FWHM equal to 10 samples and with $\beta = 0.05$. The error ratio is $\epsilon = 0.076$ and 0.120 for $N_z = 60$ and $N_z = 40$, respectively. For the small FOV ($N_z = 20$) the DBP reconstruction with noisy data and unknown density failed.

With the examples in figures 6 and 7, the density c was underestimated by the DBP algorithm when the field-of-view was small or when the data were noisy. The bias is due to the nonlinearity of the system of equations (10)–(12). The sign of the bias is determined by the curvature of the solution $\hat{c} = C(g'_\phi(0), g''_\phi(0), p(0, \phi - \pi/2))$ to equation (10)–(12). In our example the dominant eigenvalues of the Hessian matrix of the function C are negative for most lines $\mathcal{L}_\phi$, leading to the observed negative bias.
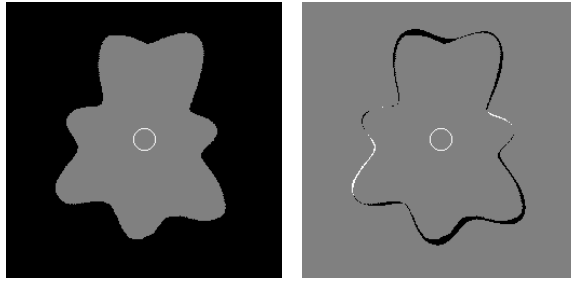
Figure 8. DBP reconstructions from noise-free data using the algorithm of section 7.1 with prior knowledge of the density, for the FOV $N_z = 20$. Left: the reconstructed star object (FOV superimposed). Right: difference between the reconstruction and the true object of figure 5.
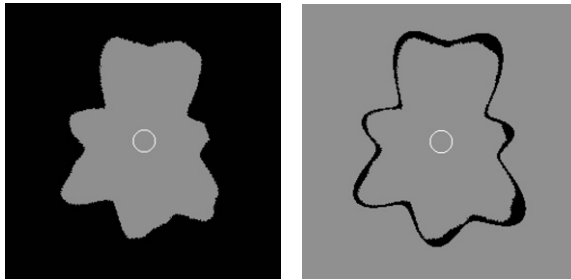
Figure 9. DBP reconstructions from noisy data using the algorithm of section 7.1 with prior knowledge of the density, for the FOV $N_z = 20$. Left: the reconstructed star object (FOV superimposed). Right: difference between the reconstruction and the true object of figure 5.

8.2. Problem 2: known density

We reconstructed the same data sets as above, now assuming that the density c is known beforehand, using both the DBP and the DART methods. For the DBP method, the knowledge of c significantly improves the stability in the presence of noise, as expected from the analysis in section 6. Results are only shown for the smallest FOV ($N_z = 20$). The DBP reconstruction from noise-free data with $\beta = 0$ is shown in figure 8. The error ratio $\epsilon = 0.064$ is much smaller than the ratio 0.233 found when the density is unknown. The DBP reconstruction from noisy data with $\beta = 0.05$ is shown in figure 9, with error ratio $\epsilon = 0.145$.

The DART reconstructions from noise-free and noisy data are shown in figures 10 and 11. Note the considerable improvement compared to the DBP algorithm in the presence of noise, with an error ratio $\epsilon = 0.0210$ instead of $\epsilon = 0.145$.

## 9. Application on real X-ray CT data of diamonds

DiamCad (Antwerp, Belgium), a diamond processing company that performs a detailed study of rough stones, scans diamonds to retrieve detailed information on their shapes. Recently, DiamCad encountered the problem that one of the diamonds was too large to be covered by the field-of-view of the detector, which resulted in truncated projection data for some of the slices. Since diamonds consist of only one material (apart from the impurities) and their shape is fairly simple, the truncated data problem forms a nice application for the proposed uniqueness theorem and DBP algorithm.
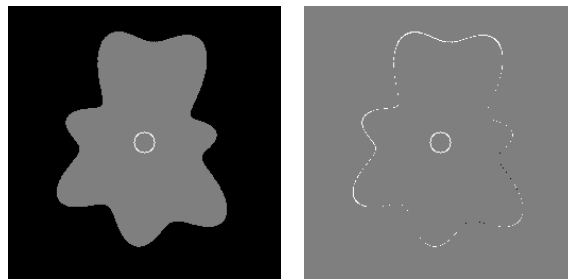
Figure 10. DART reconstruction from the same noise-free data as in figure 8, with prior knowledge of the density and a FOV $N_z = 20$. Left: the reconstructed star object (FOV superimposed). Right: difference between the reconstruction and the true object of figure 5. $\epsilon = 0.0132$.
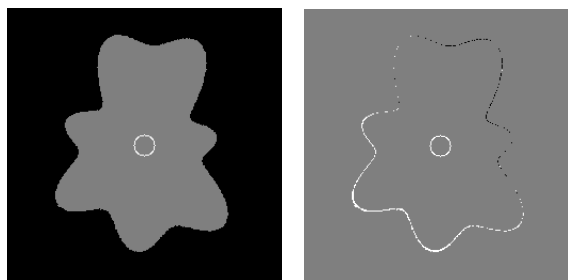

Figure 11. DART reconstruction from the same noisy data as in figure 9, with prior knowledge of the density and a FOV $N_z = 20$. Left: the reconstructed star object (FOV superimposed). Right: difference between the reconstruction and the true object of figure 5. $\epsilon = 0.0201$.
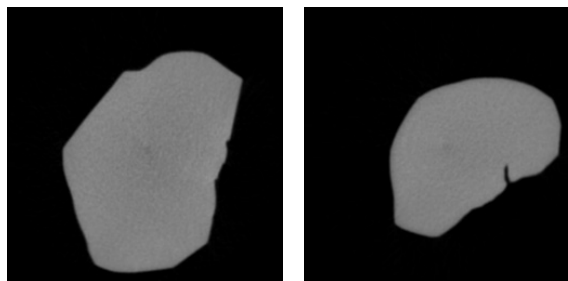
Figure 12. FBP reconstructions from non-truncated X-ray data of a diamond. Left: slice A. Right: slice B.

A diamond was scanned at 70 kVp in a Scanco μCT 40 (Scanco Medical, Brüttisellen, Switzerland) with a circular cone beam geometry. The data are recorded at 256 angles in $[0, \pi)$ using a 1024×56 (transaxial $\times$ axial) pixel detector. To cover the full axial length of the object, 500 circular cone beam scans are performed at equally spaced axial positions. The data are linearized to avoid data inconsistencies due to beam hardening. Afterwards, the data are rebinned to parallel beam, yielding a 1024×256 sized sinogram per slice, and then downsampled to 256×256 sinograms. For this results section, a star-shaped slice *A* and a nearly star-shaped slice *B* of the diamond are selected of which the full sinograms are available. The FBP reconstructions of these slices are shown in figure 12.
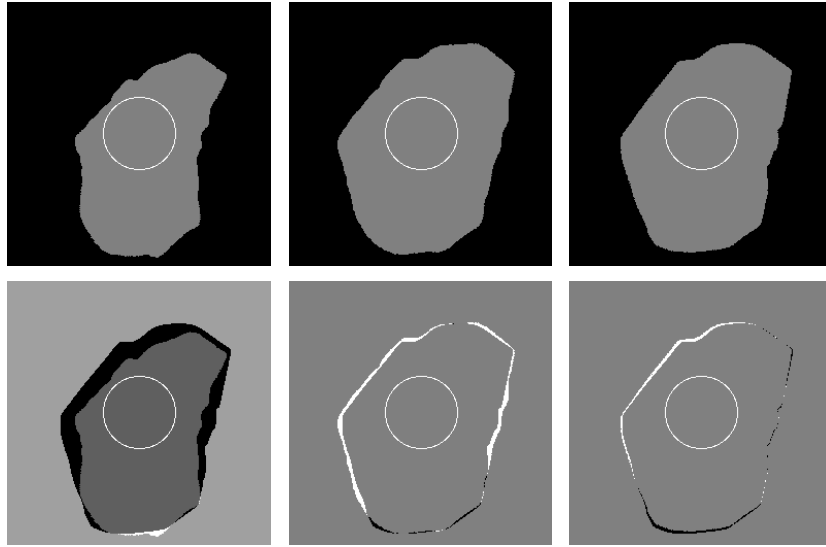
Figure 13. Reconstructions from truncated X-ray data of Slice A with a FOV diameter of $N_z = 70$. The columns correspond from left to right to the DBP reconstruction with unknown density, and the DBP and DART reconstructions with known density. The estimated density in the left reconstruction is $\hat{c} = 0.2048$. Upper row: the reconstructed diamond slice (FOV superimposed). Bottom row: difference between the reconstruction and our 'ground truth' FBP reconstruction image from complete data in figure 12.

The accuracy of the interior reconstructions is evaluated with respect to ground truth uniform images obtained by performing the histogram-based segmentation procedure of Otsu [25] of these FBP reconstructions. This segmentation also yields the density value $c = 0.346$.

The measured sinograms of slices A and B were artificially truncated so as to obtain an interior FOV with radius $N_z = 70$ radial pixels. Both truncated datasets are reconstructed using the DBP method without prior knowledge of the density c, and using the DBP and DART methods assuming that the density c is known beforehand. Figure 13 shows the respective reconstructions and their difference images for diamond slice A. Figure 14 shows the corresponding reconstructions for slice B. The DBP reconstructions are performed using $\beta = 0.05$. The error ratios of the reconstructions are shown in table 1 for both slices A and B.

Similarly to the observations for the simulated data, the DBP reconstruction where the density c is known outperforms the DBP reconstruction method with unknown c for both slices. For slice A, the DART reconstruction with known density provides the smallest error ratio, while for Slice B, the error ratios of the DBP and DART methods with known density are similar. Note however, that in the reconstruction obtained with the DART method, the non-star-shaped crack of the diamond is found, which is of course impossible for the DBP using the current description of the method.

10. Conclusion

We have shown that a star-shaped 2D object with uniform but unknown density is determined by its integrals along all lines intersecting an interior field-of-view. To the best of our knowledge this uniqueness theorem is new. The uniqueness proof is based on the relation between the backprojection of the derivative of the data and the Hilbert transform of the object along a
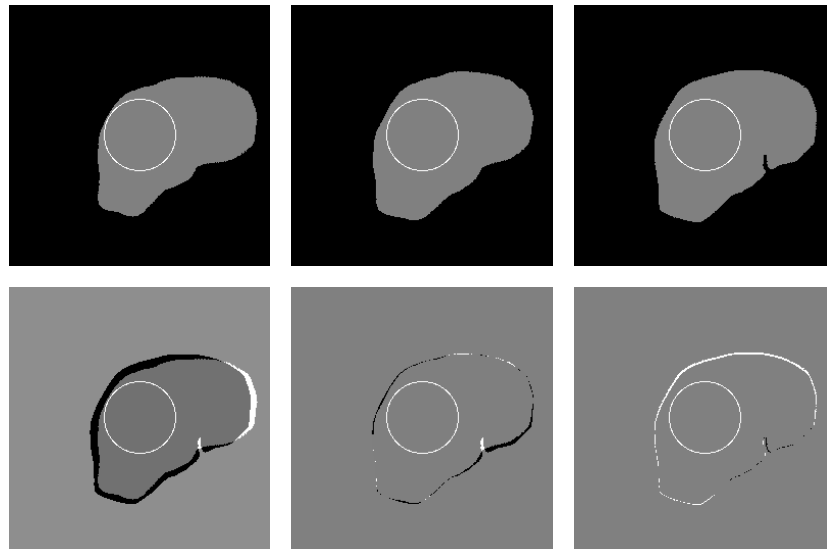
Figure 14. Reconstructions from truncated X-ray data of Slice B with a FOV diameter of $N_z = 70$. The columns correspond from left to right to the DBP reconstruction with unknown density, and the DBP and DART reconstructions with known density. The estimated density in the left reconstruction is $\hat{c} = 0.276$. Upper row: the reconstructed diamond slice (FOV superimposed). Bottom row: difference between the reconstruction and our 'ground truth' FBP reconstruction image from complete data in figure 12.

Table 1. Error ratio values ϵ of slices A and B using the DBP method without known density, and using the DBP and DART method with known $c = 0.346$.

ϵ	Slice A	Slice B
DBP without density knowledge	0.198	0.126
DBP with known $c = 0.346$	0.057	0.032
DART with known $c = 0.346$	0.0329	0.032

family of central lines. This proof is constructive and leads to a numerical algorithm, which handles each radial line independently.

This algorithm was applied to simulated and measured x-ray projections to illustrate how the stability of the reconstruction depends on the size of the interior field-of-view and on the presence of noise. One limitation of this work is that only a single noisy data set was studied, but this case-study shows a dramatic degradation of the stability as the radius of the interior field-of-view decreases. This degradation is predicted by the Cramer–Rao lower bound for the variance of the estimated density and shape of the star object, but a more systematic study will be needed to verify and quantify this property. Stability was improved to some extent by using a two-step algorithm and by filtering the noisy data in the angular variable. Additional regularization might be achieved, for instance by improving the calculation of the data derivative in the first step of the algorithm. However an optimal stability requires a global two-dimensional approach, which avoids separating the reconstruction into a set of one-dimensional reconstructions along central lines. This was illustrated using the DART algorithm for the case where the density is known beforehand.

The uniqueness result in section 4 is derived and illustrated for a 2D star-shaped object, but the approach could be extended by noting that the DBP reduces the reconstruction problem to the inversion of the truncated Hilbert transform along a family of central lines. This reduction is valid for arbitrary objects and also for the 3D x-ray transform, and we therefore conjecture that uniqueness might also hold for uniform objects with more complex shapes. Stability however is likely to worsen with increasing complexity. The investigation of these generalizations will be the subject of future work.

Acknowledgments

References

[1] Gardner R J 2006 *Geometric Tomography* 2nd edn (Cambridge: Cambridge University Press)
[2] Gardner R J 1995 Geometric tomography *Not. AMS* **42** 422–9
[3] Volčič A 1986 A three-point solution to Hammer's x-ray problem *J. Lond. Math. Soc.* **34** 349–59
[4] Hsieh J 2003 *Computed Tomography, Principles, Design, Artifacts and Recent Advances* (Bellingham, WA: SPIE Press)
[5] Natterer F and Wubeling F 2001 Mathematical methods in image reconstruction *SIAM Monographs on Mathematical Modeling and Computation* (Philadelphia: SIAM)
[6] Maass P 1992 The interior radon transform *SIAM J. Appl. Math.* **52** 710–24
[7] Ye Y, Yu H, Wei Y and Wang G 2007 A general local reconstruction approach based on a truncated Hilbert transform *Int. J. Biomed. Imag.* 2007(1) Article ID 63634
[8] Kudo H, Courdurier M, Noo F and Defrise M 2008 Tiny *a priori* knowledge solves the interior problem in computed tomography *Phys. Med. Biol.* **53** 2207–31
[9] Gelfand I M and Graev M I 1991 Crofton's function and inversion formulas in real integral geometry *Funct. Anal. Appl.* **25** 1–5
[10] Noo F, Clackdoyle R and Pack J D 2004 A two-step Hilbert transform method for 2D image reconstruction *Phys. Med. Biol.* **49** 3903–23
[11] Zou Y, Pan X and Sidky E Y 2005 Image reconstruction in regions-of-interest from truncated projections in a reduced fan-beam scan *Phys. Med. Biol.* **50** 13–28
[12] Pack J D, Noo F and Clackdoyle R 2005 Cone-beam reconstruction using the backprojection of locally filtered projections *IEEE Trans. Med. Imag.* **24** 70–85
[13] Zhuang T, Leng S, Nett B E and Chen G-H 2004 Fan-beam and cone-beam image reconstruction via filtering the backprojection image of differentiated projection data *Phys. Med. Biol.* **49** 5489–503
[14] Zou Y and Pan X 2004 Exact image reconstruction on PI-lines from minimum data in helical cone-beam CT *Phys. Med. Biol.* **49** 941–59
[15] Defrise M, Noo F, Clackdoyle R and Kudo H 2006 Truncated Hilbert transform and image reconstruction from limited data *Inverse Problems* **22** 1037–53
[16] Batenburg K J and Sijbers J 2007 DART: a fast heuristic algebraic reconstruction algorithm for discrete tomography *Proc. ICIP* **4** 133–6
[17] Candes E, Romberg J and Tao T 2006 Robust uncertainty principles: exact signal reconstruction from highly incomplete frequency information *IEEE Trans. Inf. Theory* **52** 489–509
[18] Sidky E, Kao C-M and Pan X 2006 Accurate image reconstruction from few-views and limited-angle data in divergent-beam CT *J. X-ray Sci. Tech.* **14** 119–39
[19] Herman G T and Davidi R 2008 Image reconstruction from a small number of projections *Inverse Problems* **24** 045011
[20] Ramm A G and Katsevich A I 1996 *The Radon Transform and Local Tomography* (Boca Raton, FL: CRC Press)
[21] Courdurier M 2007 Restricted measurements for the x-ray transform *PhD Thesis* University of Washington
[22] Tricomi F G 1957 *Integral Equations* (New York: Dover) p 1985
[23] Barrett H H and Myers K J 2004 *Foundation of Image Science* (New York: Wiley)

[24] Joseph P M 1982 An improved algorithm for reprojecting rays through pixel images *IEEE Trans. Med. Imag.* **1** 192–6

[25] Otsu N 1979 A threshold selection method from gray level histograms *IEEE Trans. Syst. Man. Cybern.* **9** 62–6

[26] Courdurier M, Noo F, Defrise M and Kudo H 2008 Solving the interior problem of computed tomography using *a priori* knowledge *Inverse Problems* **24** 065001

[27] Solmon D C 1976 The X-ray transform *J. Math. Anal. Appl.* **56** 61–83